1 **A polymer gel index-matched to water enables diverse applications in fluorescence**
2 **microscopy**
3

4 Xiaofei Han[1,2*,^], Yijun Su[1,3*,^], Hamilton White[4,5*,^], Kate M. O'Neill[6, 7], Nicole Y. Morgan[8], Ryan
5 Christensen[1], Deepika Potarazu[1], Harshad D. Vishwasrao[3], Stephen Xu[1], Yilun Sun[9], Shar-yin
6 Huang[9], Mark W. Moyle[10], Qionghai Dai[2], Yves Pommier[9], Edward Giniger[6], Dirk R. Albrecht[4,11,]
7 [&], Roland Probst[12, &], Hari Shroff[1, 3, 13, &]
8

9 1. Laboratory of High Resolution Optical Imaging, National Institute of Biomedical Imaging
10   and Bioengineering, National Institutes of Health, Bethesda, Maryland, USA
11 2. Department of Automation, Tsinghua University, 100084, Beijing, China
12 3. Advanced Imaging and Microscopy Resource, National Institutes of Health, Bethesda,
13   Maryland, USA
14 4. Department of Biomedical Engineering, Worcester Polytechnic Institute, 100 Institute
15   Road, Worcester, MA, 01609, USA
16 5. Department of Neurobiology, University of Massachusetts Medical School, Worcester,
17   MA 01655, USA
18 6. National Institute of Neurological Disorders and Stroke, NIH, Bethesda, MD, 20892, USA.
19 7. Institute for Physical Science and Technology, University of Maryland College Park,
20   College Park, Maryland, USA
21 8. National Institute of Biomedical Imaging and Bioengineering, National Institutes of
22   Health, Bethesda, Maryland, USA
23 9. Developmental Therapeutics Branch and Laboratory of Molecular Pharmacology, Center
24   for Cancer Research, National Institutes of Health, Bethesda, Maryland, USA
25 10. Department of Neuroscience and Department of Cell Biology, Yale University School of
26   Medicine, New Haven, CT 06536, USA.
27 11. Department of Biology and Biotechnology, Worcester Polytechnic Institute, 100 Institute
28   Road, Worcester, MA, 01609, USA.
29 12. ACUITYnano, Innovation in Biomedical Imaging, North Bethesda, Maryland, USA
30 13. Marine Biological Laboratory Fellows Program, Woods Hole, MA, USA
31

32 *Equal contribution
33 & Equal contribution
34 ^ Correspondence to hxftsinghua@126.com, suy4nih@gmail.com, hawhite@wpi.edu
35

36 **Abstract**
37

38 We demonstrate diffraction-limited and super-resolution imaging through thick layers (tens-
39 hundreds of microns) of BIO-133, a biocompatible, UV-curable, commercially available polymer
40 with a refractive index (RI) matched to water. We show that cells can be directly grown on BIO-
41 133 substrates without the need for surface passivation and use this capability to perform
42 extended time-lapse volumetric imaging of cellular dynamics 1) at isotropic resolution using
43 dual-view light-sheet microscopy, and 2) at super-resolution using instant structured

1

44   illumination microscopy. BIO-133 also enables immobilization of 1) *Drosophila* tissue, allowing
45   us to track membrane puncta in pioneer neurons, and 2) *Caenorhabditis elegans*, which allows
46   us to image and inspect fine neural structure and to track pan-neuronal calcium activity over
47   hundreds of volumes. Finally, BIO-133 is compatible with other microfluidic materials, enabling
48   optical and chemical perturbation of immobilized samples, as we demonstrate by performing
49   drug and optogenetic stimulation on cells and *C. elegans*.
50
51   **Introduction**
52
53   Fluorescence microscopy spurs biological discovery, especially if imaging is performed at
54   high spatiotemporal resolution and under physiologically relevant conditions. Coupling
55   fluorescence microscopy with strategies for immobilizing or confining samples enables further
56   applications, particularly when studying organisms that move rapidly. For example, the
57   transparency and genetic accessibility[1] of the nematode *C. elegans* has made it an ideal system
58   for studying the growth, morphology and function of individual cells in the context of the whole
59   organism[2,3]; yet imaging the living animal without motion blur usually requires immobilization
60   with chemical[4,5], steric[6,7], or microfluidic[8-11] means.
61   Microfluidic systems provide efficient immobilization and handling[12-18] for studying
62   cellular morphology[19,20] and dynamics[21], neuronal function[22-24], behavior[25-27], and lifespan[28,29].
63   Hydrogels (either independently[7,30] or in conjunction with microfluidics[31]) have also been
64   demonstrated as highly useful materials with tunable mechanical[32], diffusive, and optical
65   properties[33] that are well-suited for long-term imaging applications[7,34,35].
66   Unfortunately, relatively few attempts have been made to index-match immobilization
67   devices[36-39]. The high refractive index (RI, n) of materials commonly used in microfluidics, such
68   as polydimethoxylsilane (PDMS), causes significant optical aberrations[40,41] due to the RI
69   mismatch that occurs at the interface between the polymer (n_{PDMS} ~ 1.41) and an aqueous
70   sample (n_{water} = 1.33). These aberrations severely degrade image focus, resolution, and signal,
71   compromising the performance of immobilization devices by reducing the information content
72   of the resulting data. Hydrogels offer a lower RI (n ranging from 1.34 – 1.41) depending on
73   thickness and polymerization conditions[33]. Although the RI of these materials is better matched
74   to living samples, even a small mismatch in RI causes a noticeable deterioration in image
75   quality[42]. Image degradation is particularly obvious when using water-dipping lenses designed
76   for imaging living samples, such as those employed in high-resolution light-sheet fluorescence
77   microscopy (LSFM)[43-45].
78   Here we demonstrate a broadly applicable refractive-index-matched specimen
79   mounting method that introduces negligible aberration when imaging living samples with high-
80   resolution light-sheet microscopy and super-resolution microscopy. We show its utility in
81   combination with microfluidics, enabling applications in high-resolution, volumetric imaging of
82   cells, *Drosophila* tissue, and *C. elegans* adults and larvae. Our method takes advantage of the
83   commercially available UV curable optical polymer BIO-133 (MY Polymers Ltd.) that has a
84   refractive index matched to water (n = 1.333), is non-fluorescent, and is non-toxic. We show
85   that 1) BIO-133 provides a gas permeable, inert, and biocompatible scaffold on which to grow
86   and image tissue culture cells, 2) enables rapid tissue or animal encapsulation, and 3) is
87   compatible with other microfluidic mounting schemes and optical or chemical perturbations.

2

88
89 **Results**
90
91 *BIO-133 does not introduce additional optical aberrations*
92
93   We assessed the optical properties of BIO-133 by using dual-view light-sheet microscopy
94 (diSPIM[43,46]) to image 100 nm yellow-green beads placed under polymer layers of progressively
95 increasing thickness (**Fig. 1, Methods**). In the most common diSPIM implementation, two
96 identical 0.8 numerical aperture (NA) water-dipping objectives mounted above a planar
97 substrate (usually a glass coverslip) alternately illuminate the sample with a light sheet and
98 detect the resulting fluorescence. Since both illumination and detection planes are angled at
99 ~45 degrees with respect to the glass coverslip, imaging through a polymer gel with surface
100 parallel to the coverslip will introduce significant lateral ('x' direction, **Fig. 1a**) and axial ('z'
101 direction, **Fig. 1a**) aberrations if the gel's refractive index differs from that of water.
102   As predicted, we observed this effect when imaging beads embedded under polymers
103 with different RIs (**Fig. 1b, c**). Under no polymer, images of beads approximate the system point
104 spread function, with measured lateral and axial full width at half maximum (FWHM) 395.9 +/-
105 7.7 nm and 1527.9 +/- 119.5 nm (*N* = 70 beads), respectively. Imaging beads under PDMS
106 caused severe aberrations (**Fig. 1c**), more than doubling the lateral FWHM under a 25 μm layer
107 (816.8 +/-24.9 nm) with progressive deterioration under thicker polymer layers (**Fig. 1b**). We
108 also observed aberrations (**Fig. 1b, c**) under poly(ethylene-glycol) diacrylate (PEG-DA)[7] and
109 fluorinated ethylene polymer (FEP)[47], albeit to lesser extent as the refractive indices of these
110 polymers are closer to water. By contrast, beads imaged under BIO-133 showed negligible
111 visual aberrations or measurable degradation in image quality (**Fig. 1b, c, Supplementary Table
112 1**), even under a 150 μm thick film, the largest thickness we tested (lateral FWHM 416.5 +/- 8.5
113 nm). We attribute this result to the refractive index of BIO-133, which we measured to be
114 1.333. We also verified, under 488 nm, 561 nm, and 637 nm illumination, that BIO-133
115 introduces negligible autofluorescence (**Supplementary Fig. 1**).
116
117 *High- and super-resolution imaging of cells through a layer of BIO-133*
118
119   BIO-133 has permeability to oxygen about 2-3 times greater than PDMS and has water
120 repellent properties (Personal Communication, Ehud Shchori, My Polymers, Ltd.). These
121 material properties are advantageous for maintaining physiologically relevant cell culture
122 conditions. Thus, we investigated whether BIO-133 could provide an inert and biocompatible
123 scaffold for single cell imaging (**Supplementary Table 2a**). After a curing and leaching treatment
124 (**Methods**), U2OS cells seeded on a 50 μm layer of BIO-133 adhered and displayed similar
125 morphology and growth rate to cells grown on glass coverslips (**Fig. 2a, Supplementary Fig. 2**).
126 Similar results were obtained using HCT-116 (human colon carcinoma) cells that express
127 endogenous topoisomerase I-GFP, and we also observed similar expression and localization of
128 tagged proteins compared to cells cultured on glass coverslips (**Supplementary Figs. 2, 3**).
129   To demonstrate that transfected cells seeded directly on BIO-133 could be imaged at
130 high spatiotemporal resolution, we created BIO-133 substrates on PDMS supports
131 (**Supplementary Fig. 4**) and imaged cells expressing mEmerald-Tomm20, a fluorescent marker

132 of the outer mitochondrial membrane, through a 50 μm thick BIO-133 layer using diSPIM (**Fig.**
133 **2b, c**). The jointly registered and deconvolved data acquired from two views displayed isotropic
134 spatial resolution (**Fig. 2c, d**), allowing us to clearly visualize individual mitochondria and their
135 dynamics (**Supplementary Video 1**), including mitochondrial fusion and fission (**Fig. 2d**). We
136 also used BIO-133 in conjunction with diSPIM to construct a simple gravity-driven flow
137 cytometry setup, obtaining clear images of DAPI stained nuclei as they flowed through the
138 chamber (**Supplementary Fig. 5, 6, Supplementary Video 2**).
139   Next, we sought to image subcellular targets at spatial resolution beyond the diffraction
140 limit, so we turned to instant structured illumination microscopy (iSIM)[48], which enables high-
141 speed super-resolution imaging. We again seeded U2OS cells expressing mEmerald-Tomm20 on
142 a 50 μm BIO-133 film, this time imaging them with iSIM using a water dipping lens in an
143 inverted geometry (**Fig. 2e**). Again, BIO-133 provided aberration-free imaging, enabling us to
144 visualize the internal mitochondrial space absent Tomm20 (**Fig. 2f, g, Supplementary Video 3**).
145 We also visualized LAMP-1-GFP-stained lysosome dynamics in wild type HCT-116 cells grown on
146 another BIO-133 film of 50 μm thickness (**Supplementary Fig. 7, Supplementary Video 4**). As a
147 third example, we grew multiple layers of HCT-116 cells on BIO-133, and immunostained the
148 cells for lamin A/C, Tomm20, and actin (**Fig. 2h**), obtaining clear images of these structures
149 through the volume of the sample (**Fig. 2i, Supplementary Video 5**). We conclude that BIO-133
150 is compatible with multicolor, super-resolution imaging in live and fixed targets.
151
152 *BIO-133 enables subcellular imaging, segmentation, and tracking within immobilized living*
153 *tissue*
154
155   In addition to monitoring the dynamics of organelles within single cells, we also
156 immobilized and imaged multicellular structures in flies and worms at high spatiotemporal
157 resolution, using diSPIM in conjunction with BIO-133 for sample immobilization (**Fig. 3,**
158 **Supplementary Table 2b**). The developing *Drosophila* wing has long been a model for axon
159 growth and neuronal pathfinding and differentiation[49,50]. More recently, spinning disk confocal
160 microscopy was used to dissect the role of cytoskeletal organization and dynamics in shaping
161 the morphogenesis and growth of the TSM1 pioneer sensory neuron axon in explanted early-
162 pupal wing imaginal discs[51,52]. In those experiments, phototoxicity and photobleaching limited
163 imaging duration to ~30 volumes, with image volumes acquired every 3 minutes. Wings were
164 sandwiched between two glass coverslips to immobilize the preparation and prevent it from
165 moving during imaging, but this scheme introduces unacceptable aberrations if imaging with
166 the less phototoxic diSPIM. Instead, we immobilized wings with a thin layer of BIO-133 (**Fig. 3a,**
167 **Supplementary Fig. 8**), which enabled sustained volumetric imaging with diSPIM. We acquired
168 360 single-view volumes (5 s inter-volume interval, spanning 30 minutes) of tdTomato-CD4
169 expressed in TSM1 and the neighboring L3 neuron, marking neuronal membranes (**Fig. 3b**). In
170 addition to observing slower remodeling of the TSM1 growth cone (**Fig. 3c, top**) our imaging
171 rate also enabled us to capture rapid movement of membrane-labeled puncta that appeared to
172 traffic along the L3 axon shaft (**Fig. 3c, bottom, Supplementary Video 6**). Puncta were also
173 evident in comparative spinning disk confocal datasets (**Supplementary Fig. 9**).
174   In another example, we used soft lithography techniques[53] to cast BIO-133 into
175 microfluidic devices suitable for trapping *C. elegans* (**Supplementary Fig. 10**). Introducing adult

4

176 worms into the channels via suction (**Fig. 3a**), we imaged fine structures (**Fig. 3d**) and functional
177 activity (**Fig. 3e-j**) in living animals at isotropic resolution. Animals were sufficiently immobile
178 that we could serially acquire and fuse the two diSPIM views[54] to obtain reconstructions free of
179 motion blur. In strains expressing GFP sparsely targeted to a few neurons, we resolved axons
180 and dendrites (likely from amphid neurons, **Fig. 3d**) within anesthetized *C. elegans*. When
181 imaging the genetically encoded calcium indicator GCaMP6s[55] and mCherry targeted pan-
182 neuronally[56] in immobilized adult animals without anesthetic, our volume imaging rate of 1.25
183 Hz (simultaneous acquisition of red and green channels) enabled us to segment and track 126
184 nuclei in the animal head (**Fig. 3e,f Supplementary Video 7**), permitting inspection of
185 spontaneously active nuclei (**Fig. 3f, g**) over our 450 volume (6 minute) experiment. Intriguingly,
186 we observed a pair of nuclei (#79 and #15, **Fig. 3e, g**) that exhibited in-phase, rhythmic activity
187 with slow (45-80 s) period (**Supplementary Video 7**), as well as nuclei showing out-of-phase
188 activity with respect to this pair (#27). In another experiment, we simply embedded *C. elegans*
189 larvae expressing the same pan-nuclear GCaMP6s marker in a cured disk of BIO-133 (**Fig. 3a**),
190 recording volumes from one side to obtain volumes at 4 Hz, for 250 volumes. Despite the
191 poorer axial resolution of single-sided imaging, and the smaller size of the larval nuclei, we were
192 able to again segment and track 110 nuclei in the head of the animal, identifying calcium
193 transients in spontaneously active nuclei with a time resolution of 0.25 s (**Fig. 3h-j,**
194 **Supplementary Video 8**).
195 　　　　The droplet-based design also enabled easy recovery of animals post-imaging. 26 / 28
196 animals were recovered even ~12 hours after embedding, confirming our suspicion that cured
197 BIO-133 is inert, gas permeable, water repellant, and does not obviously affect animal viability
198 (the remaining two animals died within the BIO-133 capsule due to internal hatching of
199 embryos within the animals). The water repellency of BIO-133 likely contributes to retaining the
200 animal's intrinsic hydration and thus viability during encapsulation. The ease at which *C.
201 elegans* can be immobilized and imaged at high spatiotemporal resolution suggests useful
202 synergy with multicolor strategies that permit unambiguous neural identification[23].
203
204 *BIO-133 is compatible with chemical and optogenetic perturbations*
205
206 　　　　The ability to specifically perturb and subsequently follow biological processes by
207 observing morphological or functional changes is valuable in dissecting biological processes.
208 We conducted several studies to show that BIO-133-mounted samples are compatible with
209 such perturbations (**Fig. 4**). First, we conducted a simple drug assay by modifying our BIO-
210 133/PDMS cellular scaffolds (**Fig. 2b, Supplementary Fig. 11**) so that U2OS cells could be
211 exposed (**Fig. 4a**) to carbonyl cyanide m-chlorophenyl hydrazine (CCCP), an inhibitor of
212 oxidative phosphorylation. Because we could clearly observe cells through the BIO-133 layer
213 using diSPIM, we observed that, compared to control cells in a neighboring well (**Fig. 4a-c**),
214 within minutes of exposure the treated cells showed mitochondrial fragmentation, eventually
215 exhibiting major disruption to the mitochondrial network (**Fig. 4b, c, Supplementary Video 9**).
216 　　　　Chemically stimulating animals directly embedded in BIO-133 is difficult, since BIO-133 is
217 not permeable to aqueous solutions. One solution is to introduce chemicals via microfluidic
218 channels (such as those shown in **Fig. 3d-g**). Alternatively, we explored using PEG-DA for
219 immobilization and aqueous permeability, above a microfluidic layer for stimulus introduction

5

220   and control, and beneath a BIO-133 layer to enclose the fluidic path. Using a thin PEG-DA disk
221   allows easy transfer of different embedded organisms on the same imaging setup, and
222   repeated imaging of the same animals over many hours if desired. We constructed a hybrid
223   multi-material device composed of a PDMS microfluidic base bonded to a BIO-133 upper
224   membrane that sealed in a small PEG-DA disk containing tens of embedded nematodes[7]
225   (**Supplementary Fig. 12, Fig. 4a**). Chemicals applied via flow channels diffuse into the PEG-DA
226   disk, evoking neural responses that can be imaged through the BIO-133 viewing layer with
227   widefield microscopy or diSPIM (**Fig. 4d-g, Methods**). We embedded 21 animals expressing
228   GCaMP2.2b in AWA chemosensory neurons[57] in a PEG-DA disk and applied 1.1 μM diacetyl
229   pulses, which directly activate these neurons via the ODR-10 chemoreceptor[57,58]. Using
230   widefield microscopy, we recorded robust calcium transients from all animals and observed a
231   characteristic sensory adaptation to repeated stimulation (**Fig. 4e**). The initiation of sensory
232   neural responses varied slightly due to diffusion of diacetyl stimulus through the PEG-DA disk to
233   animals embedded in different planes (**Supplementary Fig. 13**). Next, we examined individual
234   neuron responses by using the same apparatus with diSPIM (**Fig. 4f,g Supplementary Video
235   10**). Our imaging provided sufficient spatial resolution to distinguish subcellular responses,
236   observing faster on and off dynamics of fluorescent transients in the dendrites than in the
237   soma[59].
238   Other stimulation modalities (such as light, temperature, and mechanical vibration) are
239   directly transmissible through BIO-133, and these can be applied directly to cells and organisms
240   embedded in the polymer in a simpler preparation. Optogenetic neural activation is a
241   particularly advantageous tool, allowing remote light-induced activation or suppression of
242   neurons. We embedded nematodes expressing the red light activated cation channel
243   Chrimson[60] and GCaMP2.2b[7] directly in BIO-133 disks and monitored calcium readout with
244   diSPIM during repeated red light stimulation pulses (**Fig. 4a,h,i, Supplementary Video 11**). We
245   observed increases in fluorescence after each stimulus (**Fig. 4h**), and again could clearly localize
246   such transients to subcellular areas including soma, dendrite, and axon (**Fig. 4i**).

247

248   **Discussion**

249

250   BIO-133 is commercially available, rapidly curing, gas permeable, inert, water repellent,
251   and biocompatible. It is not autofluorescent under visible illumination and does not introduce
252   additional aberration when imaging with water-dipping or water-immersion objective lenses
253   designed for aqueous specimens. These characteristics make it well-suited to microfluidic
254   experiments under physiological conditions, particularly with the many LSFM systems that use
255   such lenses. We suspect that capillary mounting[47], often used for mounting zebrafish in LSFM,
256   could be improved if BIO-133 were used instead of the FEP material commonly used in this
257   application. Our finding that cells can be directly grown on BIO-133 without additional surface
258   treatment may prove useful in non-standard LSFM geometries that previously employed RI-
259   matched materials with passivated surfaces[45], or in ultra-high-throughput light-sheet
260   imaging[61,62].
261   We also found that BIO-133 does not noticeably degrade imaging performed in more
262   traditional inverted microscope geometries, including in super-resolution imaging. This
263   capability suggests that using BIO-133 could improve imaging in studies of cell morphology,

6

264   mechanics, migration, and motility, e.g., when using micropillars[20,63] or in traction force
265   microscopy[64].
266   We bonded BIO-133 to glass and PDMS with silicone-based adhesive tape, or reversibly
267   to glass via van der Waals forces. The elastic modulus of cured BIO-133 (5 MPa) is similar to that
268   of PDMS (3.7 MPa). Thus, similar to PDMS[65], BIO-133 conforms to minor imperfections in glass
269   and bonds to it by weak van der Waal forces, creating a reversible bond and a watertight
270   seal. We suspect further tuning of adhesive, optical and mechanical properties of this intriguing
271   polymer is possible but will depend on knowing the chemical formula, which is currently
272   proprietary.
273
274   **Author Contributions**
275
276   Conceived project: R.P., H.S. Designed experiments: X.H., Y.S., H.W., K.M.O., H.D.V., E.G., D.A.,
277   R.P., H.S. Provided technical advice and resources for microfluidics: N.M., R.P., H.W., D.A.
278   Provided biological advice: R.C., Y.S., S.H., Y.P. Created new reagents: S.H., Y.P, M.W.M.
279   Performed experiments: X.H., Y.S., H.W., K.M.O., D.P., H.D.V., R.P. Tracked nuclei in GCaMP
280   imaging experiments: X.H., Y.S., S.X. Wrote paper with input from all authors: X.H., Y.S., H.W.,
281   D.A., R.P., H.S. Supervised research: Q.D., Y.P., E.G., D.A., R.P., H.S. Directed research: H.S.
282
283   **Acknowledgements**
284

296
297   **Disclaimer:** The NIH, its officers, and staff do not recommend or endorse any company,
298   product, or service.
299
300   **Methods**
301
302   **Sample preparation**
303
304   *U2OS, wild type (WT) HCT-116, and HCT-116 TOP1-GFP cell culture*
305   U2OS (ATCC, HTB-96), WT HCT-116 (ATCC, CCL-247), and HCT-116 TOP1-GFP (see below) cells
306   were cultured in DMEM (Lonza, 12-604F) media with 10% Fetal Bovine Serum at 37° C and 5%
307   CO_2.

7

308
309   To tag the genomic topoisomerase I (TOP1) in WT HCT-116 cells, sequence
310   CCTCACTTGCCCTCGTGCCT targeting a CRISPR site 77nt after the stop codon of TOP1 was cloned
311   into pX330. Homology arms (of ~1 kb) upstream and downstream of the target site were cloned
312   to flank a blasticidin‐resistance gene, where the upstream homology arm was modified to
313   replace the stop codon with a GFP domain connected to the protein-coding region of the last
314   exon of TOP1 via a short poly-lysine linker. Both constructs were co-transfected into WT-
315   HCT116 cell, followed by selection with 5 μg/mL of blasticidin 48 hours post transfection. GFP-
316   positive cells were further selected by FACS.
317
318   *Transfection of cells*
319   Cells were cultured to 50% confluency and transfected using xTreme Gene HP DNA Transfection
320   Reagent (Sigma, 6366236001). The transfection mixture contained 100 μL 1X PBS, 2 μL
321   Transfection Reagent, and 200-1000 ng plasmid DNA. Cells were imaged 24-48 hours after
322   transfection.
323
324   *C. elegans samples*
325   Nematode strains were grown on NGM plates seeded with OP50 bacteria. *C. elegans* imaged as
326   young adults were synchronized by picking L4 stage worms 24 hours prior to the experiment
327   and transferring them to seeded plates, and *C. elegans* imaged as larvae were directly picked
328   from plates. Strain DCR6268 (*olaEx3632[pttx-3b::SL2::Pleckstrin homology domain::GFP::unc-54*
329   *3'UTR + pelt-7::mCh::NLS::unc-54 3'UTR]*) was used for imaging axons and dendrites (**Fig. 3d**).
330   olaEx3632 was made by injecting plasmid DACR2285 (pttx-3b::SL2::Pleckstrin homology
331   domain::GFP::unc-54 3'UTR) at 25 ng/uL and DACR2436 (pelt-7::mCh::NLS::unc-54 3'UTR) at 10
332   ng/μL. Strain AML32[56] (*wtfIs5 [rab-3p::NLS::GCaMP6s + rab-3p::NLS::tagRFP]*) was used for pan-
333   nuclear neuronal calcium imaging (**Fig. 3e-j**); strain NZ1091(*kyIs587 [gpa-6p::GCaMP2.2b; unc-*
334   *122p::dsRed]; kyIs5662 [odr-7p::Chrimson:SL2:mCherry; elt-2p::mCherry][7]*) was used for
335   chemical (**Fig. 4d-g**) and optogenetic stimulation (**Fig. 4h, i**) . For optogenetic stimulation, L4
336   stage animals were transferred to agar plates seeded with 62.5 μM all trans-retinal (ATR, Sigma
337   Aldrich, R2500) for over 12 hours.
338
339   *Drosophila samples*
340   *Drosophila* stocks were obtained from the Bloomington *Drosophila* Stock Center: *neur-GAL4*
341   (BL6393) and *UAS-CD4-td-Tomato* (BL35837). White prepupae were selected and aged for 13-
342   14 h at 18°C followed by 1 h at 25°C (equivalent to 7.5–8 h at 25°C). These aged pupae were
343   dissected in fresh culture media (CM; Schneider's Drosophila media + 10% fetal bovine serum,
344   both from Life Technologies), and wing discs were isolated from the aged pupae and stored in
345   fresh CM prior to mounting with BIO-133.
346
347
348   **Characterizing the optical properties of polymers**
349
350   *Characterization of aberrations by visualizing fluorescent beads under different polymer layers*

8

351   100 nm diameter yellow-green fluorescent beads (Invitrogen, F8803, 1:10000 dilution in water)
352   were coated on #1.5 coverslips (24 mm x 50 mm, VWR, 48393-241) coated with 0.1% w/v poly-
353   L-lysine (Sigma, P8920-100ML). We placed spacers (Precision Brand, 44910) of variable
354   thickness on one of the coverslips and deposited droplets of BIO-133, 10% PEG-DA (ESIBIO,
355   GS705) or UV-curable PDMS (Shin-Etsu Chemical, KER-4690) on the beads. The droplet was
356   then covered with another coverslip coated with beads and compressed with an iron ring. BIO-
357   133 and PEG-DA hydrogels were crosslinked at 312 nm (Spectroline ENB-280C) for 2 minutes.
358   PDMS was crosslinked at 312 nm for 5 minutes and post-cured at room temperature for one
359   day. Once cured, we separated the two cover glasses and kept the one with polymer/hydrogel
360   on it. For imaging through FEP films of different thickness (CS Hyde, 23-1FEP-24, 25 μm; 23-
361   2FEP-24, 50 μm; 23-3FEP-24, 75 μm; 23-5FEP-24, 125 μm), we immersed beads in 1μL water
362   and covered the sample with the FEP film. All bead images were acquired with a symmetric
363   0.8/0.8 NA diSPIM[43].
364
365   *Measurement of refractive index of polymers*
366   A refractometer (American Optical) was used to measure the refractive index of pure water,
367   BIO-133 film (My Polymer, BIO-133, 25 μm), PDMS film (Shin-Etsu Chemical, KER-4690, 25 μm),
368   FEP film (CS Hyde, 23-1FEP-24, 25 μm), and 10% PEG-DA hydrogel (100 μm). The refractive
369   index for each material was measured 3 times and the average value reported in **Fig. 1**.
370
371   *Measurement of BIO-133 autofluorescence*
372   A 50 μm thick BIO-133 film was deposited on a glass bottom dish (MatTek, P35G-1.5-14-C).
373   Images were acquired both on the BIO-133 area and an area without BIO-133, using an instant
374   structured illumination microscope (iSIM[48]) with 40 ms exposure time and 45 mW 488 nm
375   excitation, 70 mW 561 nm excitation, or 90 mW 639 nm excitation (measured with a power
376   meter immediately prior to the objective). Care was taken to ensure the illumination was
377   focused within the BIO-133 film. The two images were subtracted to measure the
378   autofluorescence of BIO-133 relative to glass (**Supplementary Fig. 1**).
379
380   **Cell growth and imaging using BIO-133 substrates**
381
382   *Fabrication of BIO-133 cell culture wells for diSPIM experiments*
383   BIO-133-sided PDMS substrates with 2.5 mm diameter wells (**Supplementary Fig. 4**) were used
384   for live cell imaging experiments (**Fig. 2b-d**). To make the BIO-133 bottom, a BIO-133 droplet
385   was positioned on a #1.5 glass coverslip (24 mm x 50 mm, VWR 48393-241) between two 50
386   μm plastic spacers (Precision Brand, 44910), covered with another coverslip , compressed with
387   a glass slide (Ted Pella, 260386) and cured with a UV lamp (365nm, Spectroline ENB-280C) for
388   15 minutes. After curing, the BIO-133 film was peeled off and exposed to UV light for another 2
389   hours in 70% ethanol. To make the PDMS well, 15 mL PDMS (Dow Inc. Sylgard 184) was poured
390   into a 10 cm plastic dish (Kord-Valmark, 2910) and cured for 2 hours at 80 °C to obtain a 2 mm
391   thick PDMS slab. We punched 2.5 mm diameter matching holes on the PDMS slab and a piece
392   of double-sided tape (Adhesives Research, ARCare 90880) using a 2.5 mm diameter circular
393   punch (Acuderm Inc., P2550). The PDMS slab and the tape were then cut into smaller pieces (~5

9

394   mm on a side) with a razor blade (Sparco, 01485). BIO-133 membranes, PDMS chunks and

395   double-sided tape were further disinfected in 70% ethanol for 2 hours. After disinfection, the

396   BIO-133 membrane was adhered to PDMS using the adhesive tape, so that the matching holes

397   became wells for cell culture. After seeding and growing cells in wells, the assembly was flipped

398   over for diSPIM imaging.

399

400   *Quantification of cell growth*

401   Cured and leached 50 μm thick BIO-133 films were deposited on glass bottom dishes (MatTek,

402   P35G-1.5-14-C). Similar aliquots of U2OS (or HCT 116 TOP1-GFP) cells were seeded onto BIO-

403   133 films or on another glass bottom dish without BIO-133 (MatTek, P35G-1.5-14-C). Dishes

404   seeded with cells were maintained between imaging experiments in an incubator at 37C, 5%

405   CO_2. On each dish, a small area was selected and imaged using a widefield microscope equipped

406   with a 10x/0.25 NA objective lens each day, for three days. Cells numbers were estimated from

407   images with the Cell Counter ImageJ plugin (https://imagej.nih.gov/ij/plugins/cell-

408   counter.html). Each experiment was repeated three times. Raw images were divided by

409   Gaussian-blurred versions of themselves (sigma = 5 pixels) to flat-field images prior to display

410   (**Fig. 2a, Supplementary Fig. 2**).

411

412   *Live cell imaging through BIO-133 with diSPIM*

413   U2OS cells were cultured and transfected with 100-200 ng of mEmerald-Tomm20 plasmid

414   (Addgene, 54281) directly on the BIO-133 bottomed well plate. The well plate was inverted and

415   immersed in live cell imaging solution (Invitrogen, A14291DJ). Cells were imaged with a

416   symmetric 0.8/0.8 NA diSPIM, through the BIO-133 layer. 50 volumes were acquired with 3 s

417   intervals between dual-view volumes. Dual-view data were jointly deconvolved with ImageJ

418   plugin DiSPIM Fusion[54], and were drift- (with ImageJ plugin Correct 3D Drift

419   (https://imagej.net/Correct_3D_Drift) and bleach- corrected (with ImageJ function Bleach

420   Correction (https://imagej.net/Bleach_Correction, exponential fitting method) prior to display.

421

422   *Super-resolution imaging through BIO-133 with iSIM*

423   U2OS or WT HCT-116 cells were cultured and transfected with mEmerald-Tomm20 or LAMP1-

424   EGFP (Taraska Lab, NHLBI) on a 50 μm thick BIO-133 film. The BIO-133 film was cured on a glass

425   bottom dish (MatTek, P35G-1.5-14-C). A 60X, NA = 1.2 water objective (Olympus, PSF grade),

426   correction collar adjusted to 0.17, was used to image the cells through the glass and BIO-133

427   film using our home built iSIM system[48] and 488 nm excitation. Volumes were acquired every 3

428   s for U2OS cells expressing mEmerald-Tomm20 and every 7 s for WT HCT-116 cells expressing

429   LAMP1-EGFP. We used an exposure time of 80 ms, and a z-step of 0.25 μm for U2OS cells and

430   0.5 μm for WT HCT-116 cells. Live HCT-116 TOP1-GFP cultured on a 50 μm thick BIO-133 film or

431   on a glass bottom dish were imaged to acquire volumes with a step size of 0.5 μm. Raw images

432   were deconvolved with the Richardson-Lucy algorithm for 20 iterations, destriped in Fourier

433   space to remove striping artifacts[66], and bleach corrected

434   (https://imagej.net/Bleach_Correction). A median filter with kernel size 0.5 pixel was applied to

435   denoise mEmerald-Tomm20 and GFP-LAMP1 images prior to display.

436

437   *Immunolabeling and imaging of multilayered WT HCT-116 cells on BIO-133*

10

438   WT HCT-116 cells were cultured on a 50 μm thick BIO-133 film on a glass bottom dish until a
439   thick layer was visible by eye. Cells were fixed with 4% paraformaldehyde (Electron Microscopy
440   Sciences) in 1X PBS for 30 minutes at room temperature (RT). Cells were rinsed 3 times in 1X
441   PBS and permeabilized with 0.1% Triton X-100/PBS (Sigma, 93443) for 15 min at RT.
442   Permeabilized cells were rinsed 3 times with 1X PBS and incubated in 1X PBS with primary
443   antibody Rabbit-α-Tomm20 (Abcam, ab186735) and Mouse-α-LaminA/C (Abcam, ab244577) at
444   a concentration of 1:100 for 1 hour at RT. After primary antibody staining, cells were washed in
445   1X PBS for 5 min, three times. Cells were stained in 1X PBS with secondary antibody Donkey-α-
446   Rabbit Alexa Fluor 488 (Jackson Immuno Research, 711-547-003), Donkey-α-Mouse JF549
447   (Novusbio, NBP1-75119JF549) and Alexa Fluor 647 Phalloidin (Thermofisher, A22287) at a
448   concentration of 1:100 for 1 hour at RT. Cells were washed in 0.1% Triton X-100/PBS for 5 min,
449   three times. In each spectral channel, 46 slices were acquired on iSIM with an exposure time of
450   100 ms and a z-step of 0.5 μm. Raw images were deconvolved with the Richardson-Lucy
451   algorithm for 20 iterations and destriped in Fourier space to remove striping artifacts[66]. The 633
452   nm channel (Alexa Fluor 647 Phalloidin) was bleach corrected
453   (https://imagej.net/Bleach_Correction) across the z stack to compensate for decreased signal
454   further into the stack.
455
456   *Flow cytometry preparation*
457   Sample handling channels, 1 mm wide and 70 μm high, were formed by pouring 20 mL PDMS
458   (Dow Corning, Sylgard 184) on a positive mold made of packaging tape (Duck Brand) cut to the
459   desired dimensions with a craft cutter (Silhouette Cameo) and stuck in a 10 cm Petri dish. A thin
460   PDMS membrane (~0.5 mm) was air plasma (Harrick Plasma, PDC-32G (115V)) bonded to the
461   channel surface. Holes at the endpoints of the channel were created by punching the PDMS
462   membrane with a 1 mm diameter circular punch (Acuderm Inc., P150) after plasma treatment.
463   A 400 μm wide (142 μm height) imaging channel was cut directly from double-sided silicon-
464   based adhesive tape (Adhesives Research, ARCare 90880) with a craft cutter and stuck to the
465   PDMS device, thus creating a connection between the two sample handling channels in the
466   lower layer. A thin BIO-133 membrane (50 μm) was placed on top of the tape to seal the
467   channel. Two thick PDMS pieces with holes (6 mm and 2 mm diameter) were cut and air plasma
468   bonded to the device to provide fluidic access. When imaging, cells were added to the 6 mm
469   diameter reservoir, and output tubing (Dow Corning, 508-004) was connected to the 2 mm
470   hole. Flow speed was adjusted by changing the height of the output tubing. See also
471   **Supplementary Fig. 5.**
472
473   *Flow cytometry imaging of fixed, DAPI-stained U2OS cells*
474   U2OS cells were fixed in 4% Paraformaldehyde/PBS and subsequently stained with DAPI in 0.1%
475   Triton X-100/PBS (Sigma, 93443). The flow device was mounted on a 10 cm petri dish for
476   imaging with diSPIM. Fixed cells were added to the input port, producing steady flow through
477   the channel after several minutes. 1000 frames of the same image plane were acquired with
478   diSPIM at 50 frames per second under 'fixed sheet mode'.
479
480   **Live animal/tissue imaging through BIO-133 with diSPIM**
481

11

482   *Live imaging of BIO-133 embedded Drosophila wings*

483   A 13 μm thick BIO-133 film was created and cut into two rectangular pieces (4.5 mm x 10 mm)

484   and a square piece (10 mm x 10 mm). The rectangular pieces were deposited on a 10 cm petri

485   dish to form a 1 mm wide open-top channel. Early pupal fly wings were deposited into the

486   channel (convex side up) with 20-40 μL culture media, the square BIO-133 piece placed on top

487   to close the channel and additional culture media was carefully added to the dish (**Fig. 3a,**

488   **Supplementary Fig. 8)**. Single-view diSPIM imaging was then performed. 360 volumes were

489   acquired with 5 s inter-volume spacing, over 30 minutes. Volumes were deconvolved with

490   MATLAB and bleach corrected with ImageJ (https://imagej.net/Bleach_Correction, exponential

491   fitting method).

492

493   *Fabrication of microfluidics for C. elegans immobilization*

494   Standard soft lithography techniques[67] were used to fabricate an SU-8 (Kayaku Advanced

495   Materials, formerly Microchem Corp.) master mold for sets of four microfluidic funnels for

496   worm confinement as described[53]. To fabricate devices in BIO-133 (MY Polymers Ltd.), we

497   placed two spacers (100 μm, Precision Brand 44910) beside the pattern, poured polymer onto

498   the mold, covered the mold with a glass slide and cured the polymer under a UV lamp (365nm,

499   Spectroline ENB-280C) for 2 minutes. After curing, we peeled the BIO-133 off the mold,

500   punched inlet and outlet holes with a 1 mm diameter circular punch (Acuderm Inc., P150), and

501   sealed the device to a #1.5 cover glass (24 mm x 50 mm, VWR 48393-241) with double-sided

502   silicone-based adhesive tape (Adhesives Research, ARCare 90880). We cut out an aperture from

503   a 10 cm petri dish and used UV-curable optical cement (Norland Products Inc., Norland Optical

504   Adhesive NOA 68) to secure the coverslip carrying the microfluidic device over the aperture in

505   the petri dish. Inlet and outlet tubing (Dow Corning, 508-004) was clamped to the assembly

506   using a pair of hollow magnets (K&J Magnetics, R211-N52) placed above and below the

507   coverslip, as described[68]. Optical cement was again used to secure tubing to the magnets. See

508   also **Supplementary Fig. 10**.

509

510   *Live imaging of C. elegans through BIO-133 chambers*

511   To load worms into the immobilization device, we added a drop of M9 buffer containing worms

512   to the inlet and created vacuum at the outlet using a syringe. Within several minutes (for a 4-

513   channel chip), worms were observed to align in the channels. The petri dish was then filled with

514   water and worms were imaged with symmetric 0.8/0.8 NA diSPIM. For structural imaging, we

515   added 0.25 mM levamisole to the buffer to stop residual worm motion. For calcium imaging,

516   the outlet was connected to a peristaltic pump (Dolomite Microfluidics, 3200243) which

517   provided negative pressure to immobilize worms without using anesthetics. We simultaneously

518   imaged nuclei structure (TagRFP) and the nuclear-localized calcium response (GCaMP) with 488

519   nm and 561 nm excitation (Coherent) and image splitting devices on the detection side

520   (Hamamatsu W-VIEW GEMINI), using a previously described fiber-coupled diSPIM system[46].

521   Dual-view stacks were acquired every 0.8 s over 500 time points. Dual-color, dual-view images

522   were deconvolved and registered with ImageJ plugin DiSPIM Fusion[54].

523

524   *Droplet-based immobilization of nematodes prior to imaging, and recovery after imaging*

525 *C. elegans* were directly transferred from agar plates into a drop (~10 µL) of BIO-133 or 10%
526 PEG-DA (ESIBIO GS705) on a #1.5 cover glass (24 mm x 50 mm, VWR, 48393-241). The droplet
527 was positioned between two 100 µm spacers (Precision Brand, 44910), and was compressed by
528 a glass slide followed by 2-minute polymerization under a UV lamp (365nm, Spectroline ENB-
529 280C). After polymerization, worms were immobilized in the resulting gel disk. The gel disk was
530 then placed in a 10 cm petri dish or a standard chamber for diSPIM imaging. Single-view stacks
531 were acquired every 0.25 s for 250 time points. After imaging, worms could be released and
532 checked for viability by gently breaking the droplet with forceps. In some experiments, we
533 immersed the disks in M9 buffer for up to 12 hours, finding that live worms could also be
534 recovered after this period.
535
536 *Tracking nuclei, calcium imaging analysis*
537 TagRFP volumes were imported into Imaris and neurons tracked with Imaris for Tracking
538 (https://imaris.oxinst.com/products/imaris-for-tracking) to obtain the center of each neuron at
539 every timepoint. A custom MATLAB script was used to extract the calcium signal. For every
540 neuron, the average intensity of TagRFP channel I_{561} and the intensity of GCaMP channel I_{488}
541 were computed by averaging pixels within a 2 µm (adult) or 1.5 µm (larval) diameter sphere
542 placed around each center position. I_{561} and I_{488} were calculated from dual-view deconvolved
543 images (Fig. 3 f, g) or single-view raw data (Fig. 3 i, j). The ratio $R=I_{488}/I_{561}$ was used to minimize
544 non-GCaMP fluctuations. Neuronal activity for the datasets in **Fig. 3** was reported as dR/R = (R −
545 R_0)/R_0, where R_0 is the baseline for an individual neuron defined as its lower 20th percentile
546 intensity value.
547
548 **Chemical and optical perturbations in BIO-133 based imaging devices**
549
550 *Fabrication of chemical delivery devices for cells*
551 A modified PDMS well plate design (**Supplementary Fig. 11**) was applied to deliver chemical
552 perturbations to cells (**Fig. 4a-c**). A 400 µm thick BIO-133 film was created using the method
553 described above. 10 mL PDMS was cured in a 10 cm dish, PDMS tubing (Dow Corning, 508-004)
554 was placed on the cured PDMS layer at 8 mm intervals, and another 15 mL PDMS was added to
555 obtain a ~4 mm thick PDMS slab with channels contained inside. Holes crossing the channels
556 were punched at 8 mm intervals using a 5 mm diameter circular punch (Acuderm Inc., P550). A
557 piece of double-sided silicone-based adhesive tape (Adhesives Research, ARCare 90880) was
558 also punched at 8 mm intervals using a 2.5 mm diameter circular punch (Acuderm Inc., P2550).
559 The PDMS slab and the tape were cut into two-well pieces. BIO-133 film, PDMS chunks and
560 double-sided tape were disinfected in 75% ethanol. After disinfection, the BIO-133 membrane
561 was adhered to PDMS via the double-sided adhesive tape, so that the matching holes became
562 wells for cell culture. After growing cells, tubing (Scientific Commodities Inc., BB31695-PE/2)
563 was inserted into both sides of the channel for introducing chemical flow and another piece of
564 double-sided tape without holes was used to seal the wells. The assembly was flipped over for
565 diSPIM imaging through the BIO-133 membrane.
566
567 *Mitochondrial imaging in the presence of CCCP*

13

568 U2OS cells were cultured in two 5 mm diameter BIO-133 bottomed wells with ports and
569 transfected with 300-400 ng of mEmerald-Tomm20. Before imaging, the wells were filled with
570 live cell imaging solution (Invitrogen, A14291DJ), flipped over and attached to a 10 cm petri dish
571 with double-sided silicone-based adhesive tape (Adhesives Research, ARCare 90880). For the
572 well containing control cells, tubing was left disconnected from a source. For the well
573 containing cells that experienced chemical perturbation, input tubing was connected to a
574 syringe containing 0.05 mM carbonyl cyanide m-chlorophenyl hydrazine (CCCP, Sigma, C2759).
575 The syringe is higher than the output tube so that drug flow was induced by gravity. We used a
576 valve (McMaster-Carr, 7033T21) placed between the input tube and syringe to control the flow.
577 The valve was closed prior to imaging. For each well, two cells were chosen for imaging. A
578 multi-position acquisition was set in the Micro-manager[69] diSPIM plugin[70] to sequentially image
579 the four cells. Volume acquisition time was 3 s, and 90 volumes were acquired for each cell with
580 60 s intervals between volumes. 10 minutes after the imaging started, the valve was opened
581 and drug flow was induced in ~60 s. Dual-view images were deconvolved with ImageJ plugin
582 DiSPIM Fusion[54], drift corrected (ImageJ plugin Correct 3D Drift,
583 https://imagej.net/Correct_3D_Drift) and bleach corrected (ImageJ function Bleach Correction,
584 https://imagej.net/Bleach_Correction, exponential fitting method).
585
586 *Encapsulation of C. elegans into PEG hydrogels*
587 *C. elegans* were encapsulated into PEG hydrogel disks as described in our prior work[7]. PEG
588 hydrogel precursor solutions were prepared by combining 20% w/v poly(ethylene glycol)
589 diacrylate (PEG-DA, 3350 MW, 94.45% acrylation, ESI BIO) with 0.10% w/v Irgacure 2959
590 photoinitiator (2-hydroxy-4'-(2-hydroxyethoxy)-2-methylpropiophenone, I2959, BASF) in 1x S-
591 basal buffer (100 mM NaCl, 50 mM KPO_4 buffer, pH 6.0). Clean 24 mm x 50 mm glass coverslips
592 (VWR) were rendered permanently hydrophobic by exposure to vapors of (tridecafluoro-
593 1,1,2,2-tetrahydrooctyl) trichlorosilane (Gelest). For covalent attachment of the PEG hydrogel
594 to glass, coverslips (Thermo Scientific) were silanized by coating with 3-(trimethoxysilyl)propyl
595 methacrylate (TMSPMA, Sigma-Aldrich). Both methods of surface modification were applied to
596 1" x 3" glass slides (VWR). A small volume (1.75 μL) of PEG hydrogel solution with photoinitiator
597 was pipetted onto a hydrophobic glass slide flanked by two PDMS spacers whose thickness
598 matched the desired hydrogel thickness of 150 μm. Animals were transferred into the hydrogel
599 solution by worm pick. A coverslip, TMSPMA treated for making mounted PEG-DA gels, or
600 untreated for making freestanding gels, was placed over the hydrogel droplet and supported by
601 the PDMS spacers. The glass slide/coverslip sandwich was then placed over a UV light source
602 (312 nm, International Biotechnologies, Inc, model UVH, 12W) and illuminated for two minutes
603 until gelation. Hydrogel disks were immediately transferred to wet agar dishes to keep
604 embedded animals hydrated.
605
606 *Fabrication of microfluidic devices for chemical stimulation of C. elegans*
607 Microfluidic chambers were prepared using poly(dimethyl siloxane) (PDMS; Sylgard 184, Dow
608 Corning) in a ratio of 1:10 and poured to a depth of 5 mm on a silicon master positive mold of
609 the microchannels used previously[71]. Once cut free of the master, devices were punched so
610 that two balanced-length inlets and the outlet had 1.5 mm holes going through the thickness of
611 the material, and 1 mm holes punched from the side to allow flexible tubing to be inserted from

14

612   the sides. The smooth PDMS device surface opposite the microchannels was irreversibly
613   bonded to a glass slide using oxygen plasma (Harrick PDC-32G, 18W, 45 seconds). A thin PDMS
614   membrane (150 μm) was cut with a 3.5 mm diameter dermal punch and then oxygen plasma
615   bonded to the microfluidic channel surface with the hole in the membrane exposing the
616   micropost array. The hole in the thin PDMS membrane formed a "well" that hydrogel disks
617   could be gently placed in with forceps. A thin BIO-133 membrane (75-80 μm) was prepared by
618   gelation of BIO-133 liquid polymer between two glass slides rendered permanently
619   hydrophobic as described above. Two layers of clear cellophane tape (height of ~80 μm)
620   formed the standoffs that determined final membrane height. After degassing the microfluidic
621   device in a vacuum chamber for approximately 45 minutes, the device was removed from the
622   desiccator, connected to tubing, and flushed with S. basal buffer before use to remove any air
623   bubbles. Hydrogel disks could be interchanged between the well formed by the PDMS above
624   the micropost array easily using forceps and then the system sealed for microfluidic flow using
625   the thin BIO-133 membrane described above. See also **Supplementary Fig. 12**.
626
627   *Preparation of Chemosensory Stimulus*
628   For both wide-field and diSPIM assays, diacetyl (2,3-butanedione, Sigma) was diluted to 1.1 μM
629   in 1x S. basal (10^{-7} dilution). 1 μL of 1 mg/mL fluorescein solution was added to 40 mL of
630   diacetyl solution to visualize stimulus delivery.
631
632   *Wide-field Imaging with Chemical Stimulation*
633   For wide-field, single plane imaging of multiple *C. elegans* at once[57], the microfluidic chamber,
634   valves, tubing and reservoirs were prepared as above and placed on a Zeiss AxioObserver
635   epifluorescence microscope with a 5x, 0.25 NA objective, EGFP filter set, and Hamamatsu Orca-
636   Flash 4 sCMOS camera. Micromanager scripts[72] automatically synchronized capture of ten 30-s
637   trials recording at 10 fps with 10 ms excitation pulses and 20 s chemical stimulation.
638   NeuroTracker software[71] analyzed the wide-field neural imaging data, from which background-
639   corrected fluorescence changes were calculated in MATLAB as $\Delta F/F_0$, where F_0 is baseline
640   neural fluorescence during the four seconds prior to stimulation. Data for multiple individual
641   animals were also presented as a population mean to show the relative decrease in average
642   calcium response after multiple stimulation periods.
643
644   *DiSPIM Imaging with Optical and Chemical Stimulation*
645   Stimulus control for optical illumination or chemical pulses was integrated with diSPIM
646   volumetric imaging using a custom Micromanager script controlling an Arduino Uno and
647   enabling independent digital switching of 6 TTL channels at the beginning of specified image
648   acquisition timepoints. One TTL channel controlled the intensity of a red LED (617 nm, 3W,
649   Mightex) connected to the bottom port of the diSPIM and illuminated the sample through a
650   Nikon 4x, 0.1 NA lower objective. A second TTL channel controlled a 12V fluidic valve system for
651   chemical stimulation (ValveLink 8.2, Automate). Pinch valves allowed flow of either buffer or
652   chemical stimulus lines into the microfluidic channel network, flowing to a common outlet.
653
654   For optogenetic stimulation experiments, animals were embedded in BIO-133 disks bonded to a
655   cover glass placed in the diSPIM sample chamber. To embed animals, they were first transiently

15

656   immobilized by being picked onto seeded (OP50 *E. coli*) plates with 1 mM tetramisole, and
657   allowed to rest for 1.5 hours. Subsequently, worms were picked into a droplet of BIO-133
658   polymer liquid and gelled in the same manner as the PEG-DA hydrogel disks above, using a
659   TMSPMA silanized coverslip for covalent bonding.
660
661   For chemical stimulation experiments, animals were embedded in PEG hydrogel disks. Animals
662   can be maintained in these disks for many hours if they are kept hydrated[7]. Just prior to an
663   experiment, an animal-embedded disk was inserted into the sample cavity of the diSPIM
664   microfluidic chamber. A 75-80 μm thick BIO-133 membrane was sealed to the microfluidic
665   device surface, closing the fluidic channel with the PEG disk and animals contained within. The
666   hydrogel disk was inserted into a droplet of S. basal buffer present in the well to avoid the
667   introduction of bubbles that would disrupt microfluidic flow. To assure continuous microfluidic
668   flow through the chamber without leaking, we balanced inlet and outlet flows by adjusting the
669   reservoir heights. Specifically, inlet reservoir heights were held slightly above the stage (Δh_{in}),
670   and the outlet reservoir level was placed further below the stage ($\Delta h_{out} > \Delta h_{in}$) to ensure a slight
671   negative pressure in the chamber. Microfluidic stimulus switching was achieved using a dual
672   pinch valve (NResearch Inc., 161P091), that alternately allows either a buffer or stimulus line to
673   flow through the microfluidic chamber to the single outflow line.
674
675   A typical diSPIM acquisition captured one volume per second (10 ms exposure, minimum slice
676   time setting, 55 slices per volume, 166.4 x 166.4 x 82.5 μm total volume space) for 10 minutes,
677   with 20-s duration stimulation every minute. Z-Projection time series videos were produced in
678   ImageJ from cropped versions of the total number of images, then analyzed for GCaMP neural
679   fluorescence using rectangular boxes for integrated fluorescence density, with a nearby region
680   void of signal used for background subtraction.
681
682

16

683
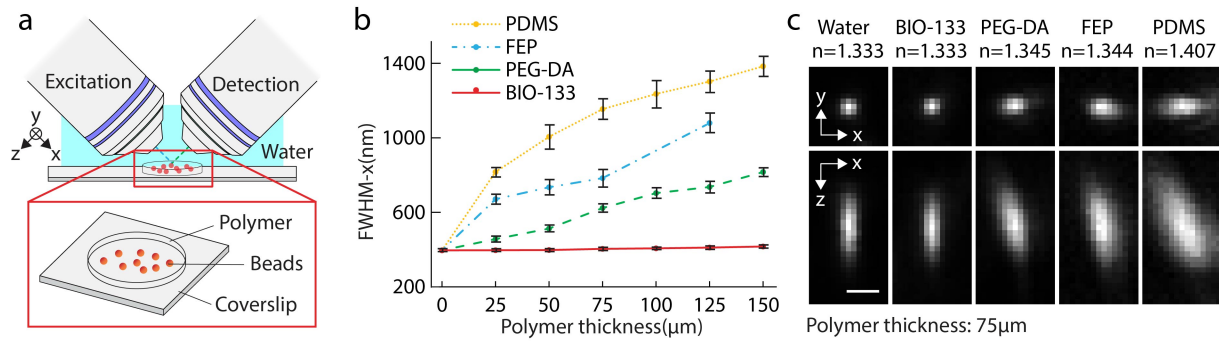
684
685

686 **Fig. 1**, **Diffraction-limited imaging is possible when imaging through BIO-133, unlike other**
687 **polymers. a)** Imaging geometry. A light sheet is used to illuminate the 100 nm yellow-green
688 bead sample, which is embedded under progressively thicker polymer. Illumination and
689 detection occur through 0.8 NA water-dipping objectives. **b)** Full width at half maximum
690 (FWHM) in the 'x' direction under different thicknesses of polymer. Means and standard
691 deviations are shown. **c)** Exemplary lateral (top row) and axial (bottom row) images of beads
692 imaged through 75 μm of polymer, demonstrating that BIO-133 provides diffraction-limited
693 performance whilst the other polymers do not. Single images, rather than maximum intensity
694 projections, are shown. The refractive index of each polymer as measured with a refractometer
695 is also indicated (average value from 3 independent trials). Scale bar: 1 μm. See also
696 **Supplementary Table 1**.

697

17

698
699
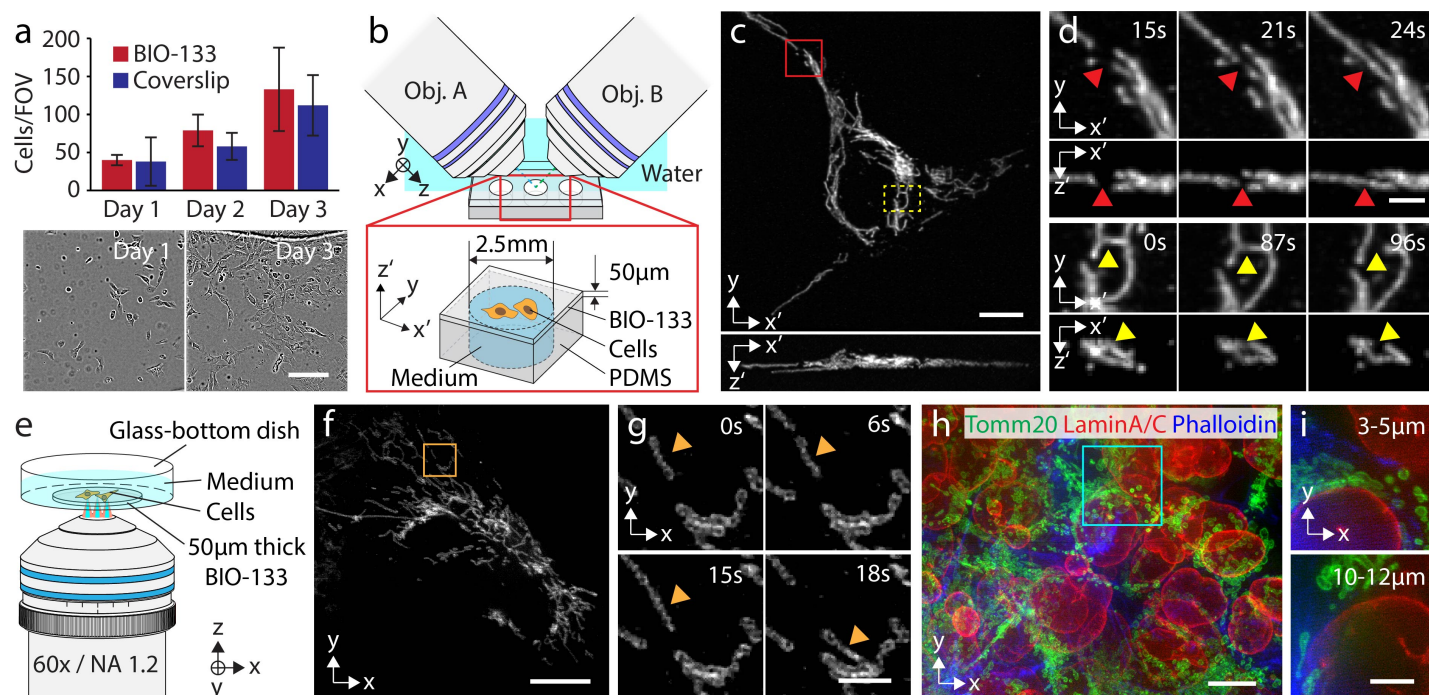
Fig. 2, BIO-133 provides an inert and biocompatible scaffold on which to grow and image cells. **a)** U2OS growth on BIO-133 is similar to growth on glass coverslips. *Top*: quantifying cell growth on 50 μm thick BIO-133 layer vs. glass coverslip. Means and standard deviations from 3 fields of view (10x magnification, ~800 μm x 800 μm field of view) are shown over 3 days. *Bottom*: example fields of view from day 1 and day 3, cells on BIO-133 layer. Scale bar: 200 μm. See also **Supplementary Fig. 2, 3**. **b)** Schematic of diSPIM imaging geometry. 50 μm film with adherent cells is inverted and imaged in the diSPIM setup. See also **Supplementary Fig. 4**. **c)** Example maximum intensity projections of deconvolved images of U2OS cells expressing mEmerald-Tomm20 in lateral (top) and axial (bottom) views. Scale bar: 10 μm. **d)**. Higher magnification views of the red and yellow rectangles in **c)**, highlighting examples of mitochondrial fusion (top, red arrowhead) and fission (bottom, yellow arrowhead). 50 volumes were taken with a 3 s inter-volume interval. See also **Supplementary Video 1**. Note that primed coordinates refer to the plane of the BIO-133 layer (x', y) and the direction normal to the BIO-133 layer (z'). Scale bar: 2 μm. **e)** iSIM imaging geometry. Cells were cultured on 50 μm BIO-133 film, and the film placed in a glass-bottom dish and immersed in cell culture medium. Imaging was performed with a 60x, NA 1.2 water-immersion lens. **f)** Example deconvolved iSIM maximum intensity projection showing live U2OS cells expressing mEmerald-Tomm20. Scale bar: 10 μm. **g)** Higher magnification view of orange rectangular region in **f)**. Orange arrowhead marks the same mitochondrion. 25 volumes were acquired with a 3 s inter-volume interval. See also **Supplementary Videos, 3, 4**. Scale bar: 2 μm. A 0.5 pixel median filter was used to denoise images in **f, g)** prior to display. **h)** Multiple layers of HCT-116 cells were grown on 50 μm BIO-133 layer and immunostained against Tomm20 (green), lamin A/C (red), and actin (blue). See also **Supplementary Video 5.** Scale bar: 10 μm. **i)** Maximum intensity projection over indicated axial range (measured from the bottom of the cell layer) for cyan rectangular region in **h)**. Scale bar: 5 μm.

18
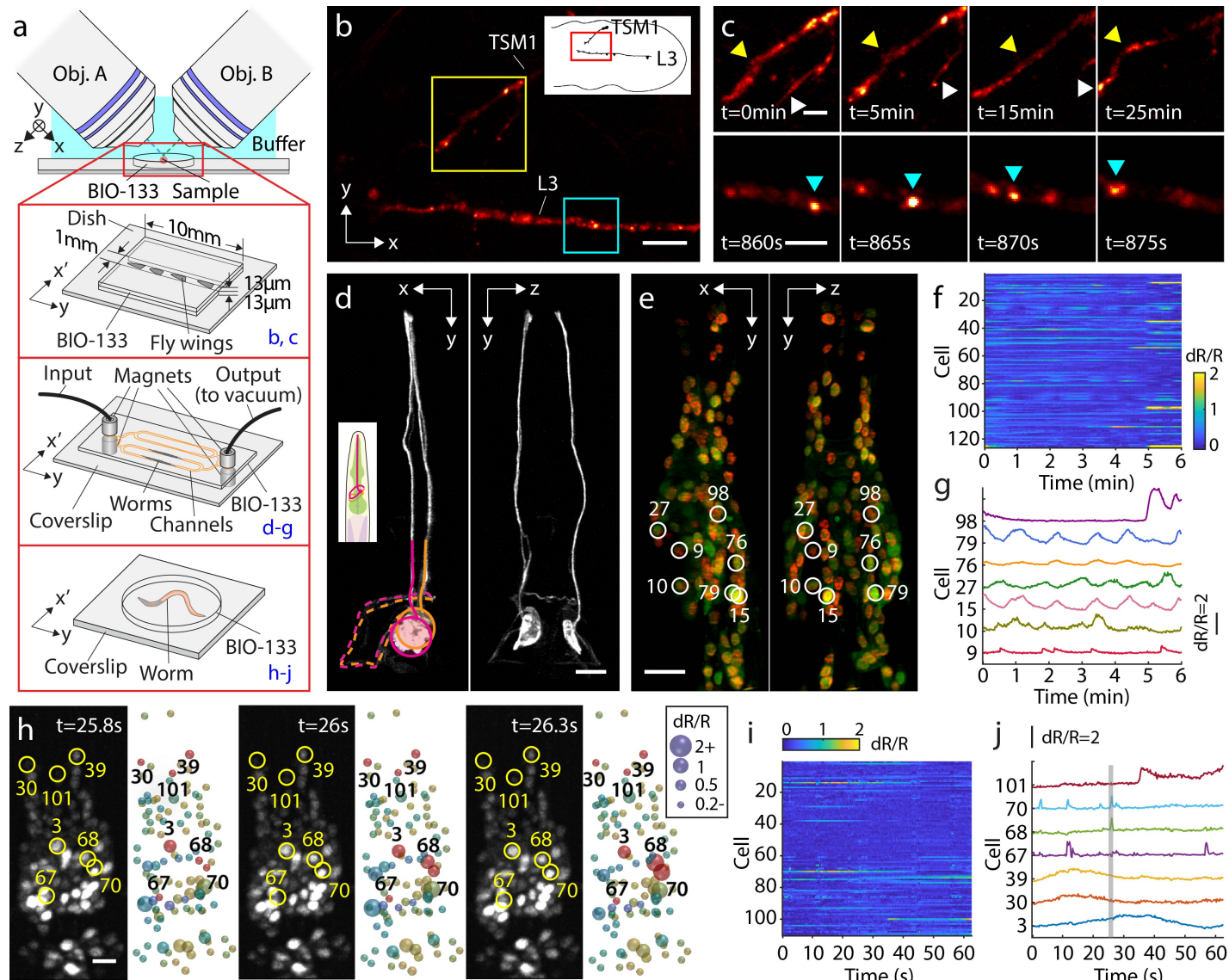
Fig. 3 Live imaging of BIO-133 encapsulated fly wings and *C. elegans*. a) Experimental schematic. Top: A thin layer of BIO-133 membrane covers excised fly wings, immobilizing them so that axon dynamics can be recorded at high resolution over an extended period. Middle: A simple microfluidic device is used to trap adult worms for structural and functional imaging of the nervous system. Bottom: Worms can also be encapsulated in a gelled droplet of BIO-133. See also **Supplementary Figs. 8, 10. b)** Deconvolved, single-view maximum intensity projection of a fly wing with TdTomato-labelled CD4 showing the axons of two neurons (upper: TSM1; lower: L3) shortly before fasciculation in the developing *Drosophila melanogaster* wing disc. Scale bar: 10 μm. 360 volumes were taken with 5 s inter-volume intervals. (30 min in total, see also **Supplementary Video 6**). **c)** Magnified regions of TSM1 and L3 axons, corresponding to yellow and blue rectangles in **b)**, highlighting morphological changes and apparent motion of CD4 puncta. Scale bars: 4 μm. **d)** Isotropic, high-resolution imaging of GFP-labeled axons and dendrites in anesthetized adult *C. elegans*, as shown by orthogonal, jointly deconvolved diSPIM maximum intensity projections. Cell bodies are circled and axons entering the nerve ring region

740   are overlaid with dotted lines. Scale bar: 10 μm. **e)** Calcium imaging of adult worm (red channel:

741   TagRFP, green channel: GCaMP6s; both labels targeted to nuclei), 2 views imaged at 1.25 Hz

742   volumetric rate. Joint deconvolution diSPIM results are shown; red and green channels were

743   simultaneously collected and colors are overlaid in display. Scalebar: 10 μm. See also

744   **Supplementary Video 7. f)** dR/R traces for all 126 tracked nuclei. **g)** dR/R traces for selected

745   individual neurons. Note correspondence with numbered neurons and marked neurons in **e). h)**

746   Calcium imaging of larval worm with higher temporal resolution (4 Hz volumetric rate), single-

747   view results are shown. GCaMP channel and associated segmented dR/R signal are indicated for

748   3 successive time points. Scale bar: 5 μm. See also **Supplementary Video 8. i)** dR/R traces for all

749   110 nuclei segmented and tracked in **h). j)** traces for selected individual neurons. Note

750   correspondence with numbered neurons and marked neurons in **h)**.

751

752

20
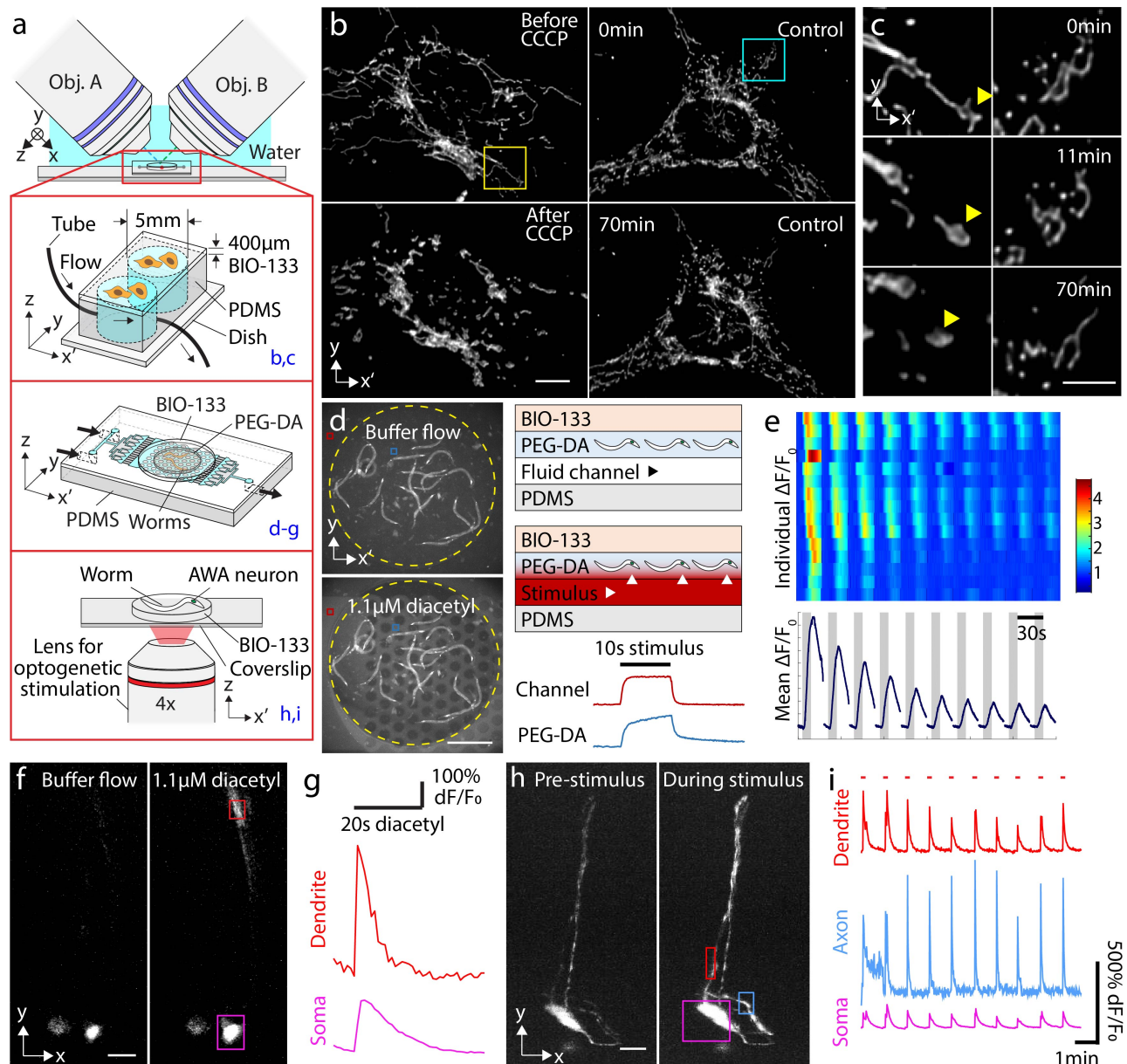
Fig. 4, BIO-133 is compatible with chemical and optical perturbations. a) Experimental schematic for perturbations. Cells grown on BIO-133 were placed on PDMS wells and were either perturbed by flowing 0.05 mM CCCP or left as controls (top higher magnification view). Alternatively, worms were embedded in PEG-DA bonded to a PDMS flow chip and imaged through a layer of BIO-133 (middle higher magnification view) to examine response to chemical stimulation; or embedded in BIO-133, repetitively stimulated with red light from lower, 4x objective and imaged using upper diSPIM objectives (bottom higher magnification view). See also **Supplementary Figs. 11-13**. **b)** Example cells with (left column) and without (right column) CCCP treatment at early (top, 0 min) and late (bottom, 70 min) time points. CCCP was added at 10 minutes. Maximum intensity projections of deconvolved diSPIM data are shown. Scale bar: 10 μm. See also **Supplementary Video 9**. **c)** Higher magnification views of yellow (left column) and blue (right column) regions in **b)**. Yellow arrowhead shows CCCP-induced morphological

766 change of mitochondrion. Scale bar: 5 μm. **d)** Example images of worms expressing GCaMP
767 immobilized in PEG-DA disk with (bottom) and without (top) 1.1 μM diacetyl. Fluorescein added
768 to stimulus highlights the rapid addition/removal of chemical. Scale bar: 500 μm. Right
769 schematics show layered structure of assembly, including direction of flow and diffusion
770 (arrowheads) into PEG-DA layer. Line plots show intensity of fluorescein over time in channel
771 (red) and PEG-DA (blue) layers. **e)** Top: dF/F heatmaps derived from widefield microscopy
772 measurements from 21 animals (rows) in response to 10 repeated stimulus pulses (once per
773 minute). Bottom: responses averaged over all animals show neural adaptation. **f)** Single-view
774 diSPIM images recorded from a single animal, showing subcellular response in AWA neuron to
775 1.1 μM diacetyl compared to control (buffer flow) conditions. Contrast has been adjusted to
776 better highlight the response from different cell regions. Scale bar: 10 μm. See also
777 **Supplementary Video 10**. **g)** Graphs show average intensity from boxed regions in **f)**
778 highlighting fluorescence intensity changes in soma and dendrite. **h)** Worms expressing
779 Chrimson and GCaMP are repetitively stimulated with red light and imaged using upper diSPIM
780 objectives. Maximum intensity projection of GCaMP fluorescence from single-view diSPIM
781 recordings are shown before (left) and after (right) optogenetic stimulation. Scale bar: 10 μm.
782 See also **Supplementary Video 11**. **i)** dF/F traces for dendrite, axon, and soma, corresponding to
783 boxed regions in **h)**.
784

References

785

786 1   Chalfie, M., Tu, Y., Euskirchen, G., Ward, W. W. & Prasher, D. C. Green fluorescent
787   protein as a marker for gene expression. *Science* **263**, 802-805 (1994).
788 2   Ou, G., Stuurman, N., D'Ambrosio, M. & Vale, R. D. Polarized Myosin Produces Unequal-
789   Size Daughters During Asymmetric Cell Division. *Science* **330**, 677-680 (2010).
790 3   Kato, S. *et al.* Global brain dynamics embed the motor command sequence of
791   Caenorhabditis elegans. *Cell* **163**, 656-669 (2015).
792 4   Chokshi, T. V., Ben-Yakar, A. & Chronis, N. CO_2 and compressive immobilization of C.
793   elegans on-chip. *Lab Chip* **9**, 151-157 (2009).
794 5   Snow, J. J. *et al.* Two anterograde intraflagellar transport motors cooperate to build
795   sensory cilia on *C. elegans* neurons. *Nature Cell Biology* **6**, 1109-1113 (2004).
796 6   Kim, E., Sun, L., Gabel, C. V. & Fang-Yen, C. Long-Term Imaging of Caenorhabditis
797   elegans Using Nanoparticle-Mediated Immobilization. *PLoS One*, e53419 (2013).
798 7   Burnett, K., Edsinger, E. & Albrecht, D. R. Rapid and gentle hydrogel encapsulation of
799   living organisms enables long-term microscopy over multiple hours. *Communications*
800   *biology* **1**, 73 (2018).
801 8   Rohde, C. B., Zeng, F., Gonzalez-Rubio, R., Angel, M. & Yanik, M. F. Microfluidic system
802   for on-chip high-throughput whole-animal sorting and screening at subcellular
803   resolution. *Proc Natl Acad Sci U S A* **104**, 13891-13895 (2007).
804 9   Cornaglia, M., Lehnert, T. & Gijs, M. A. M. Microfluidic systems for high-throughput and
805   high-content screening using the nematode Caenorhabditis elegans. *Lab Chip* **17**, 3736-
806   3759 (2017).
807 10   Berger, S. *et al.* Long-term *C. elegans* immobilization enables high resolution
808   developmental studies in vivo. *Lab Chip* **18**, 1359-1368 (2018).
809 11   Mondal, S. *et al.* Large-scale microfluidics providing high-resolution and high-throughput
810   screening of Caenorhabditis elegans poly-glutamine aggregation model. *Nat Commun.* **7**,
811   13023 (2016).
812 12   Levario, T. J., Zhan, M., Lim, B., Shvartsman, S. Y. & Lu, H. Microfluidic trap array for
813   massively parallel imaging of Drosophila embryos. *Nat Protoc.* **8**, 721-736 (2013).
814 13   Yanik, M. F., Rohde, C. B. & Pardo-Martin, C. Technologies for micromanipulating,
815   imaging, and phenotyping small invertebrates and vertebrates. *Annu Rev Biomed Eng*
816   **13**, 185-217 (2011).
817 14   Shorr, A. Z., Sönmez, U. M., Minden, J. S. & LeDuc, P. R. High-throughput
818   mechanotransduction in Drosophila embryos with mesofluidics *Lab Chip* **19**, 1141-1152
819   (2019).
820 15   Stavrakis, S., Holzner, G., Choo, J. & DeMello, A. High-throughput microfluidic imaging
821   flow cytometry. *Current Opinion in Biotechnology* **55**, 36-43 (2018).
822 16   Probst, R., Cummins, Z., Ropp, C., Waks, E. & Shapiro, B. Flow Control of Small Objects
823   On-Chip: Manipulating Live Cells, Quantum Dots, and Nano-Wires. *IEEE Control Systems*
824   *Magazine* **32**, 26-53 (2012).
825 17   Riba, J., Schoendube, J., Zimmermann, S., Koltay, P. & Zengerle, R. Single-cell dispensing
826   and 'real-time' cell classification using convolutional neural networks for higher
827   efficiency in single-cell cloning. *Scientific Reports* **10**, 1193 (2020).

23

828   18   Anagnostidis, V. *et al.* Deep learning guided image-based droplet sorting for on-demand
829   selection and analysis of single cells and 3D cell cultures *Lab Chip* **20**, 889-900 (2020).
830   19   Lam, J. *et al.* Adaptation of a Simple Microfluidic Platform for High-Dimensional
831   Quantitative Morphological Analysis of Human Mesenchymal Stromal Cells on
832   Polystyrene-Based Substrates. *SLAS Technol.* **22**, 646-661 (2017).
833   20   Doolin, M. T. & Stroka, K. M. Integration of Mesenchymal Stem Cells into a Novel
834   Micropillar Confinement Assay. *Tissue Engineering Part C: Methods* **25**, 662-676 (2019).
835   21   Albrecht, D. R. *et al.* Microfluidics-integrated time-lapse imaging for analysis of cellular
836   dynamics. *Integrative Biology* **2**, 278-287 (2010).
837   22   Reilly, D. K., Lawler, D. E., Albrecht, D. R. & Srinivasan, J. Using an Adapted Microfluidic
838   Olfactory Chip for the Imaging of Neuronal Activity in Response to Pheromones in Male
839   *C. Elegans* Head Neurons. *JoVE* **127**, e56026 (2017).
840   23   Yemini, E. *et al.* NeuroPAL: A Neuronal Polychromatic Atlas of Landmarks for Whole-
841   Brain Imaging in *C. elegans*. *bioRxiv*, https://doi.org/10.1101/676312 (2019).
842   24   Cáceres, I. d.-C., Valmas, N., Hilliard, M. A. & Lu, H. Laterally Orienting *C. elegans* Using
843   Geometry at Microscale for High-Throughput Visual Screens in Neurodegeneration and
844   Neuronal Development Studies. *PLoS One* **7**, e35037 (2012).
845   25   Albrecht, D. R. & Bargmann, C. I. High-content behavioral analysis of Caenorhabditis
846   elegans in precise spatiotemporal chemical environments. *Nat Methods* **8**, 599-605
847   (2011).
848   26   Belfer, S. J. *et al.* Caenorhabditis-in-Drop Array for Monitoring *C. elegans* Quiescent
849   Behavior. *Sleep* **36**, 689-698 (2013).
850   27   Scholz, M., Lynch, D. J., Lee, K. S., Levine, E. & Biron, D. A scalable method for
851   automatically measuring pharyngeal pumping in *C. elegans*. *Journal of Neuroscience*
852   *Methods* **274**, 172-178 (2016).
853   28   Atakan, H. B., Cornaglia, M., Mouchiroud, L., Auwerx, J. & Gijs, M. A. M. Automated
854   high-content phenotyping from the first larval stage till the onset of adulthood of the
855   nematode Caenorhabditis elegans. *Lab Chip* **19**, 120-135 (2018).
856   29   Hulme, S. E. *et al.* Lifespan-on-a-chip: microfluidic chambers for performing lifelong
857   observations of C. elegans. *Lab Chip* **10**, 589-597 (2010).
858   30   Hwang, H., Krajniak, J., Matsunaga, Y., Benian, G. M. & Lu, H. On-demand optical
859   immobilization of *Caenorhabditis elegans* for high-resolution imaging and
860   microinjection. *Lab Chip* **14**, 3498-3501 (2014).
861   31   Krajniak, J. & Lu, H. Long-term high-resolution imaging and culture of *C. elegans* in chip-
862   gel hybrid microfluidic device for developmental studies. *Lab Chip* **10**, 1862-1868 (2010).
863   32   S., N., Stowers, R., Lou, J., Xia, Y. & Chaudhuri, O. Varying PEG density to control stress
864   relaxation in alginate-PEG hydrogels for 3D cell culture studies *Biomaterials* **200**, 15-24
865   (2019).
866   33   Zhang, Z. F., Ma, X., Wang, H. & Ye, F. Influence of polymerization conditions on the
867   refractive index of poly(ethylene glycol) diacrylate (PEGDA) hydrogels. *Applied Physics A*
868   **124**, 283 (2018).
869   34   Wevers, N. R. *et al.* High-throughput compound evaluation on 3D networks of neurons
870   and glia in a microfluidic platform. *Scientific Reports* **6**, 38856 (2016).

24

871 35 Pittman, W. E., Sinha, D. B., Zhang, W. B., Kinser, H. E. & Pincus, Z. A simple culture
872   system for long-term imaging of individual *C. elegans*. *Lab Chip* **17**, 3909-3920 (2017).
873 36 Kim, D. N. H., Kim, K. T., Kim, C., Teitell, M. A. & Zangle, T. A. Soft lithography fabrication
874   of index-matched microfluidic devices for reducing artifacts in fluorescence and
875   quantitative phase imaging. *Microfluidics and Nanofluidics* **22** (2017).
876 37 Polanco, E. R., Western, N. & Zangle, T. A. Fabrication of Refractive-index-matched
877   Devices for Biomedical Microfluidics. *J Vis Exp* **139**, 58296 (2018).
878 38 Levario, T. J., Insley, P., Hwang, H., Shaham, S. & Lu, H. in *18th International Conference
879   on Miniaturized Systems for Chemistry and Life Sciences, MicroTAS 2014*   727-729 (San
880   Antonio, TX, 2014).
881 39 Xu, T. *et al.* Modified inverted selective plane illumination microscopy for
882   submicrometer imaging resolution in polydimethylsiloxane soft lithography devices. *Lab
883   Chip* **Advance Online Publication**, doi:https://doi.org/10.1039/D0LC00598C (2020).
884 40 Chang, T.-Y., Pardo-Martin, C., Allalou, A., Wählby, C. & Yanik, M. F. Fully automated
885   cellular-resolution vertebrate screening platform with parallel animal processing. *Lab
886   Chip* **12**, 711-716 (2012).
887 41 Tonin, M., Descharmes, N. & Houdré, R. Hybrid PDMS/glass microfluidics for high
888   resolution imaging and application to sub-wavelength particle trapping. *Lab Chip* **16**,
889   465-470 (2016).
890 42 Turaga, D. & Holy, T. E. Miniaturization adn defocus correction for objective-coupled
891   planar illumination microscopy. *Optics Letters* **33**, 2302-2304 (2008).
892 43 Wu, Y. *et al.* Spatially isotropic four-dimensional imaging with dual-view plane
893   illumination microscopy. *Nat Biotechnol.* **31**, 1032-1038 (2013).
894 44 Chen, B. C. *et al.* Lattice light-sheet microscopy: imaging molecules to embryos at high
895   spatiotemporal resolution. *Science* **346**, 1257998 (2014).
896 45 Hedde, P. N., Malacrida, L., Ahrar, S., Siryaporn, A. & Gratton, E. sideSPIM - selective
897   plane illumination based on a conventional inverted microscope. *Biomedical Optics
898   Express* **8**, 3918-3937 (2017).
899 46 Kumar, A. *et al.* Dual-view plane illumination microscopy for rapid and spatially isotropic
900   imaging. *Nature Protocols* **9**, 2555-2573 (2014).
901 47 Kaufmann, A., Mickoleit, M., Weber, M. & Huisken, J. Multilayer mounting enables long-
902   term imaging of zebrafish development in a light sheet microscope. *Development* **139**,
903   3242-3247 (2012).
904 48 York, A. G. *et al.* Instant super-resolution imaging in live cells and embryos via analog
905   image processing. *Nat Methods* **10**, 1122-1126 (2013).
906 49 Murray, M. A., Schubiger, M. & Palka, J. Neuron Differentiation and Axon Growth in the
907   Developing Wing of *Drosophila melanogaster*. *Developmental Biology* **104**, 259-273
908   (1984).
909 50 Jan, Y. N., Ghysen, A., Christoph, I., Barbel, S. & Jan, L. Y. Formation of Neuronal
910   Pathways in the Imaginal Discs of *Drosophila melanogaster*. *The Journal of Neuroscience*
911   **5**, 2453-2464 (1985).
912 51 Clarke, A. *et al.* Dynamic Morphogenesis of a Pioneer Axon in *Drosophila* and Its
913   Regulation by Abl Tyrosine Kinase. *Mol Biol Cell* **31**, 452-465 (2020).

25

914 52 Clarke, A. *et al.* Abl Signaling Directs Growth of a Pioneer Axon in *Drosophila* by Shaping
915 the Intrinsic Fluctuations of Actin. *Mol Biol Cell* **31**, 466-477 (2020).
916 53 Hulme, S. E., Shevkoplyas, S. S., Apfeld, J., Fontana, W. & Whitesides, G. A
917 Microfabricated Array of Clamps for Immobilizing and Imaging *C. Elegans*. *Lab Chip* **7**,
918 1515-1523 (2007).
919 54 Guo, M. *et al.* Rapid image deconvolution and multiview fusion for optical microscopy.
920 *Nature Biotechnol.*, in press, doi:https://doi.org/10.1038/s41587-020-0560-x (2020).
921 55 Chen, T.-W. *et al.* Ultra-sensitive fluorescent proteins for imaging neuronal activity.
922 *Nature* **499**, 295-300 (2013).
923 56 Nguyen, J. P., Linder, A. N., Plummer, G. S., Shaevitz, J. W. & Leifer, A. M. Automatically
924 tracking neurons in a moving and deforming brain. *PLoS Comput Biol.* **13**, e1005517
925 (2017).
926 57 Larsch, J., Ventimiglia, D., Bargmann, C. I. & Albrecht, D. R. High-throughput imaging of
927 neuronal activity in Caenorhabditis elegans. *PNAS* **110**, E4266-4273 (2013).
928 58 Sengupta, P., Chou, J. H. & Bargmann, C. I. odr-10 Encodes a Seven Transmembrane
929 Domain Olfactory Receptor Required for Responses to the Odorant Diacetyl. *Cell* **84**,
930 899-909 (1996).
931 59 Shidara, H., Hotta, K. & Oka, K. Compartmentalized cGMP Responses of Olfactory
932 Sensory Neurons in *Caenorhabditis elegans*. *Journal of Neuroscience* **37**, 3753-3763
933 (2017).
934 60 Klapoetke, N. C. *et al.* Independent optical excitation of distinct neural populations.
935 *Nature Methods* **11**, 338-346 (2014).
936 61 Martin, C. *et al.* Line excitation array detection fluorescence microscopy at 0.8 million
937 frames per second *Nature Communications* **9**, 4499 (2018).
938 62 Han, Y. *et al.* Cameraless high-throughput three-dimensional imaging flow cytometry.
939 *Optica* **6**, 1297-1304 (2019).
940 63 Ravasio, A., Vaishnavi, S., Ladoux, B. & Viasnoff, V. High-resolution imaging of cellular
941 processes across textured surfaces using an index-matched elastomer. *Acta Biomater.*
942 **14**, 53-60 (2015).
943 64 Xiao, F., Wen, X., Tan, X. H. M. & Chiou, P.-Y. Plasmonic micropillars for precision cell
944 force measurements across a large field-of-view *Appl. Phys. Lett.* **112**, 033701 (2018).
945 65 Duffy, D. C., McDonald, J. C., Schueller, O. J. & Whitesides, G. M. Rapid Prototyping of
946 Microfluidic Systems in Poly(dimethylsiloxane). *Anal Chem* **70**, 4974-4984 (1998).
947 66 Guo, M. *et al.* Single-shot super-resolution total internal reflection fluorescence
948 microscopy. *Nature Methods* **15**, 425-428 (2018).
949 67 Xia, Y. & Whitesides, G. M. Soft Lithography. *Angew. Chem. Int. Ed. Engl.* **37**, 550-575
950 (1998).
951 68 Atencia, J. *et al.* Magnetic connectors for microfluidic applications *Lab Chip* **10**, 246-249
952 (2010).
953 69 Edelstein, A. D. *et al.* Advanced methods of microscope control using μManager
954 software. *Journal of Biological Methods* **1**, e11 (2014).
955 70 Ardiel, E. L. *et al.* Visualizing Calcium Flux in Freely Moving Nematode Embryos. *Biophys.*
956 *J.* **112**, 1975-1983 (2017).

26

957   71   Lagoy, R. C. & Albrecht, D. R. Microfluidic Devices for Behavioral Analysis, Microscopy,
958   and Neuronal Imaging in Caenorhabditis elegans. *Methods Mol Biol.* **1327**, 159-179
959   (2015).
960   72   Lagoy, R. C. & Albrecht, D. R. Automated fluid delivery from multiwell plates to
961   microfluidic devices for high-throughput experiments and microscopy. *Sci. Reports* **8**,
962   6217 (2018).
963